

Article

Insight into the Behavior of Mortars Containing Glass Powder: An Artificial Neural Network Analysis Approach to Classify the Hydration Modes

Fouad Boukhelf ^{1,*}, Daniel Lira Lopes Targino ^{1,2} , Mohammed Hichem Benzaama ¹,
Lucas Feitosa de Albuquerque Lima Babadopulos ²  and Yassine El Mendili ^{1,3} 

¹ Builders Lab, Builders Ecole d'Ingénieurs, ComUE NU, 1 rue Pierre et Marie Curie, 146110 Epron, France

² Graduate Program in Civil Engineering—Structures and Civil Construction (PEC), Department of Structural Engineering and Civil Construction (DEECC), Technology Center (CT), Federal University of Ceará (UFC), Bloco 733, Campus do Pici s/n, Fortaleza 60440-900, CE, Brazil

³ Institut de Recherche en Constructibilité IRC, Ecole Spéciale des Travaux Publics, 28 Avenue du Président Wilson, 94234 Cachan, France

* Correspondence: fouad.boukhelf@builders-ingenieurs.fr; Tel.: +33-231-463-202

Abstract: In this paper, an artificial neural network (ANN) model is proposed to predict the hydration process of a new alternative binder. This model overcomes the lack of input parameters of physical models, providing a realistic explanation with few inputs and fast calculations. Indeed, four mortars are studied based on ordinary Portland cement (CEM I), cement with limited environmental impact (CEM III), and glass powder (GP) as the cement substitution. These mortars are named CEM I + GP and CEM III + GP. The properties of the mortars are characterized, and their life cycle assessment (LCA) is established. Indeed, a decrease in porosity is observed at 90 days by 4.6%, 2.5%, 12.4%, and 7.9% compared to those of 3 days for CEMI, CEMIII, CEMI + GP, and CEMIII + GP, respectively. In addition, the use of GP allows for reducing the mechanical strength in the short term. At 90 days, CEMI + GP and CEMIII + GP present a decrease of about 28% and 57% in compressive strength compared to CEMI and CEMIII, respectively. Nevertheless, strength does not cease increasing with the curing time, due to the continuous pozzolanic reactions between $\text{Ca}(\text{OH})_2$ and silica contained in GP and slag present in CEMIII as demonstrated by the thermo-gravimetric (TG) analysis. To summarize, CEMIII mortar provides similar performance compared to mortar with CEMI + GP in the long term. This can later be used in the construction sector and particularly in prefabricated structural elements. Moreover, the ANN model used to predict the heat of hydration provides a similar result compared to the experiment, with a resulting R^2 of 0.997, 0.968, 0.968, and 0.921 for CEMI, CEMIII, CEMI + GP, and CEMIII + GP, respectively, and allows for identifying the different hydration modes of the investigated mortars. The proposed ANN model will allow cement manufacturers to quickly identify the different hydration modes of new binders by using only the heat of hydration test as an input parameter.

Keywords: artificial neural network; data processing; cement; glass powder valorization; life cycle assessment



Citation: Boukhelf, F.; Targino, D.L.L.; Benzaama, M.H.; Lima Babadopulos, L.F.d.A.; El Mendili, Y. Insight into the Behavior of Mortars Containing Glass Powder: An Artificial Neural Network Analysis Approach to Classify the Hydration Modes. *Materials* **2023**, *16*, 943. <https://doi.org/10.3390/ma16030943>

Academic Editor: Malgorzata Ulewicz

Received: 20 December 2022

Revised: 14 January 2023

Accepted: 16 January 2023

Published: 19 January 2023



Copyright: © 2023 by the authors. Licensee MDPI, Basel, Switzerland. This article is an open access article distributed under the terms and conditions of the Creative Commons Attribution (CC BY) license (<https://creativecommons.org/licenses/by/4.0/>).

1. Introduction

With a production of about $10 \text{ Gm}^3/\text{year}$, concrete is the most important building material and is, therefore, responsible for some of the world's environmental problems due to the production of more than 4 billion tons/year of cement, which requires production temperatures higher than 1450 °C [1,2]. Indeed, concrete is responsible for 4 to 8% of the world's CO_2 emissions at all stages of production with 50% of the emissions in the construction sector alone [3,4]. Among materials, only coal oil and gas are a more important source of greenhouse gases [5].

One of the reflections that have emerged in recent decades is the substitution of part of the cement by other alternative binders, the supplementary cementitious materials (SCMs), with similar characteristics to cement, especially the pozzolanic and the hydration reactivities. The reduction in cement manufacturing's carbon footprint remains a challenge and will have a strong appeal in the coming years.

Once glass becomes waste, it is landfilled, which is not sustainable, because it does not decompose in the environment. The recovery of glass waste eliminates the unnecessary consumption of limited landfill areas and can reduce energy consumption, among others. As a result, it is necessary to seek solutions that are more environmentally friendly. One of the proposed solutions is to replace part of the Portland cement, the most polluting component of concrete, with wastes and by-products, while trying to keep similar mechanical characteristics. Several industrial by-products have been successfully used as SCMs, including silica fume (SF), ground granulated blast furnace slag (GGBFS), and fly ash (FA) [6–8]. These materials are used to create blended cements that can improve concrete's early durability and/or long-term strength, workability, and cost.

Glass powder (GP), which is studied in this paper, could also be a relevant solution for the creation of less- CO_2 -emitting concrete due to its high pozzolanic properties [9–12]. Each year, millions of tons of glass waste are generated worldwide [13,14]. In addition to reducing the amount of cement in concrete, glass waste will be recycled. This could be an important step toward sustainable development [15,16]. Furthermore, glass powder provides additional performance in terms of workability [17], microstructure properties [18,19], mechanical strength performance in the long term [20–22], durability [23], and hygrothermal performance [16,24,25].

In addition, in the context of sustainable applications of industrial by-products in environmentally friendly cementitious binders, Life Cycle Analysis (LCA) is a suitable tool for assessing the environmental impacts of cement production and its associated supply chains [26]. Assessing a literature review of LCA for the concrete and cementitious materials, it is seen that the major pollutant component is ordinary Portland cement (OPC), mainly due to the clinker manufacturing process. Indeed, there are three main steps for the cement manufacturing (cf., Figure 1): (i) the pre-processing, where the raw materials are crushed and milled into a fine powder; to enter the preheater; (ii) the calcination, where temperatures greater than $1400\text{ }^\circ\text{C}$ are achieved, forming the clinker; (iii) finally, the addition of gypsum to control the setting time followed by final grinding to transform the clinker into a fine-grained mixture (90% of the particles diameter are on the order of 10 microns).

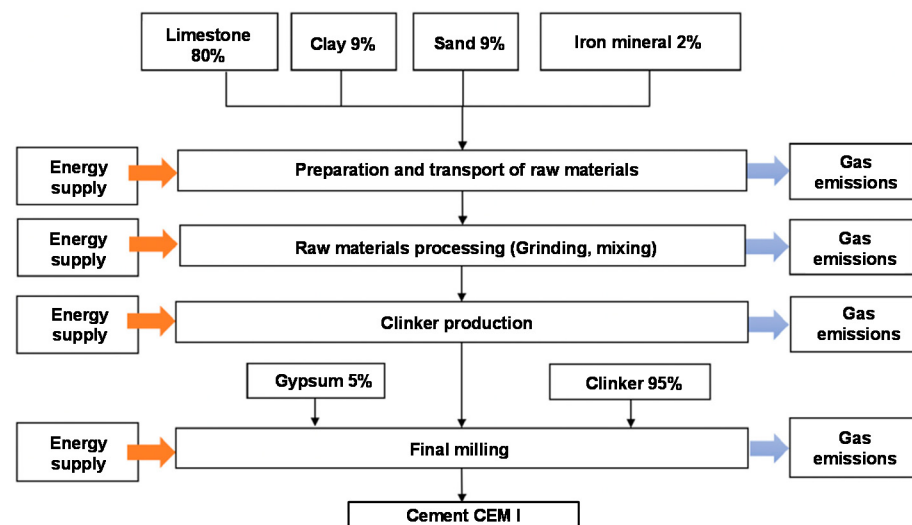


Figure 1. Basic process, “cradle-to-gate” scope and system limits [27].

The main steps of the LCA assessment are: (i) determining the scope and limitations of OPC production and its partial replacement by more environmentally friendly SCMs, evaluating greenhouse gas emissions, and energy and raw material consumption; (ii) selecting output and input data using literature reviews to obtain average values for each necessary parameter [27–33], (iii) using the input data in the evaluation of the environmental impact of the mixtures proposed in this study by preceding the interpolation, and (iv) finally, presenting the results in terms of the decrease or increase in greenhouse gas emissions and energy and raw material consumption. The regulatory parameters of the two cements used, among others, are presented in Table 1, which includes the two types of cement used in this study (CEM I and CEM III). Indeed, the mineral content of CEM I is mainly pure gypsum ($\text{CaSO}_4 \cdot 2\text{H}_2\text{O}$) with a maximum content of 5%, which controls setting time. Regarding CEM III, it contains GGBFS with a content between 36 and 95%. The current LCA assessment will be divided into three types of raw materials (i.e., clinker, GGBFS, and GP).

Table 1. Cement regulations following European Standard (EN 197-1) [27].

Class	Mineral Content		Mineral Components/Inorganic Process Additions	Market Share
	(Allowable Range)	(Average)		
Ordinary Portland cement (CEM I)	≤5%	2.5%	inorganic process addition	30%
Portland composite cement (CEM II)	6–35%	20.5%	ground granulated blast furnace slag (GGBFS), silica fume, pozzolan, fly ash, burnt shale	57%
Blast furnace cement (CEM III)	36–95%	65.5%	GGBFS	5%
Pozzolanic cement (CEM IV)	11–55%	33%	silica fume, pozzolan, fly ash	6%
Composite cement (CEM V)	36–80%	58%	GGBFS, pozzolan, fly ash	3%

To investigate the hydration kinetics of these alternative binders, several models have been proposed in the literature over recent decades. The hydration heat models are dependent on several variables, some of which are uncontrollable. Finding a credible model that accurately describes the hydration heat is a challenging task. Based on the literature, the simulation methods can be classified into three categories: (i) linear regression models [34], (ii) physical models [35], and (iii) intelligent computing models. The linear regression models are constructed by using the least-squares methods to fit experimental data under the assumption that there are linear (or nonlinear) and independent relationships between the heat of hydration and its influencing factors, i.e., cement compositions, hydration age, and cement fineness. In the work of Qin [34], the non-assumptive projection pursuit regression method has been applied to predict the hydration heat of Portland cement.

Concerning the physical models, several models have been proposed in the literature to predict cement hydration heat. Tahersima et al. [35] used a finite element model to predict the hydration heat in a concrete slab-on-grade floor with limestone blended cement. The results showed that the prediction accuracy of finite element results is about 15% more for the maximum temperature rise and 30% more for the peak time. However, the main difficulty of this model lies in the determination of the thermal properties of the material to feed the model. Furthermore, the calculation time takes longer due to discretization. Kondo et al. [36] proposed a single-particle model that considers the circular-shaped layered growth of a uniform thickness of hydrates on a spherical single-reaction cement particle to characterize the hydration kinetics of alite (C_3S). Pommersheim et al. [37,38] suggested an integrated single-particle reaction-diffusion model for the hydration of C_3S . The hydration was modeled by using a classical approach to deal with reactions and diffusion at phase boundaries.

Recently, He et al. [39] developed a numerical method to describe the hydration heat characteristics of Portland cement under atmospheric steam curing conditions. This model has been employed using an iterative algorithm and confirmed with the experimental results. More recently, Nguyen et al. [40] investigated the effects of cement particle distribution on the hydration process of cement paste using a three-dimensional cement hydration computer simulation. The hydration process of cement paste was simulated using the model based on the CEMHYD3D code and the random distribution method was simpler

and required less time in generating a pre-hydrated model than the correlation function method. In the work of Chu et al. [41], the CEMHYD3D code was also used to numerically model the hydration of cement paste by following the evolution of all phases and predicting the properties of hydrated cements. Furthermore, Zhao et al. [42] studied the early-age hydration of blended cement and modeled its hydration kinetics by measuring the hydration heat. Within this paper, the classification of hydration modes was discussed based on the Krstulovic–Dabic model [43,44], which was built on the data from the hydration rate. The limitations of numerical methods listed above indicate that there is a knowledge gap that needs to be filled, particularly for machine learning methods.

Indeed, intelligent computing models are usually based on artificial neural networks (ANN) and can also be used to assess the complicated process [45–48]. Nevertheless, a lack of knowledge on ANN applications to predict the hydration process was detected. Based on a literature review, limited works on Machine Learning (ML) and ANN applications applied to thermal data analysis and processing have been found in the literature. In addition, only two studies highlight the use of ANN models to investigate the hydration heat of Portland cement [49,50]. Subasi et al. [50] used a new approach based on an adaptive neuro-fuzzy inference system (ANFIS). Cook et al. [49] used a Random Forest (RF) model to achieve high-accuracy predictions of time-dependent thermal hydration kinetics of OPC-based analysis. Indeed, the largest drawback of RF is that it can become too slow and ineffective for real-time forecasts if there are too many combined decision trees. In general, these algorithms are quick to learn but take a long time to produce predictions after they have been trained. Moreover, ANFIS has a significant processing cost due to its complicated structure and gradient learning. This is a major drawback for applications with a high amount of data [51].

Due to the wide range of factors that influence the performance of the binder hydration process, the dynamic simulation of the hydration is a difficult task. Several variables influence heat hydration and they can occasionally be beyond control. It can be difficult to find a model that accurately describes the behavior of materials as they hydrate. Indeed, complex and non-linear systems influenced by their environment define behavior dynamics. However, the identification of the thermal parameters of the material to feed the model is where the main challenge of the physical models is presented in the literature. In addition, the discretization lengthens calculation times. For this reason, in this paper, an ANN model was used to predict the hydration process. The general objective is to fill the information gap and to present a dynamic model that can overcome the mentioned obstacles, compared to physical models, such as providing a realistic explanation of the heat of hydration, with minimum inputs and faster calculations. In order to contribute on that matter, the aims of this work were: (i) to assess the environmental impact of binders used and highlight the potential of glass powder (GP) valorization in the reduction in cement's carbon footprint; (ii) to investigate the effect of GP on the hydration heat, and on the microstructural and mechanical properties of mortars, in addition to the thermogravimetric analysis results; (iii) to propose a numerical approach to identify and classify the transition modes of the cement hydration process. For this last purpose, a multilayer perceptron regressor (MLP) was proposed to generate a smooth curve model adjusted to the data reading signal and to map each experimental dataset. This method provides an interpolated model with less noise and/or other interferences. Once validated, the numerical analysis of the generated model was used to identify the transition modes. This identification was based on local maxima and minima of the generated shape format [52–55]. This method allows the development of a reliable model that can identify and set the hydration process [56].

2. Materials and Methods

Following the approach presented in Figure 2, the methodology employed in this paper is based on experimental and numerical steps. Each phase is made up of multiple sub-steps, as detailed in the following subsections. The first step concerns the materials characterizations at the laboratory scale and their carbon footprint assessment. The second

step focuses on the data processing aspects and the general proposed numerical model dedicated to assessing the hydration process of the mortars used.

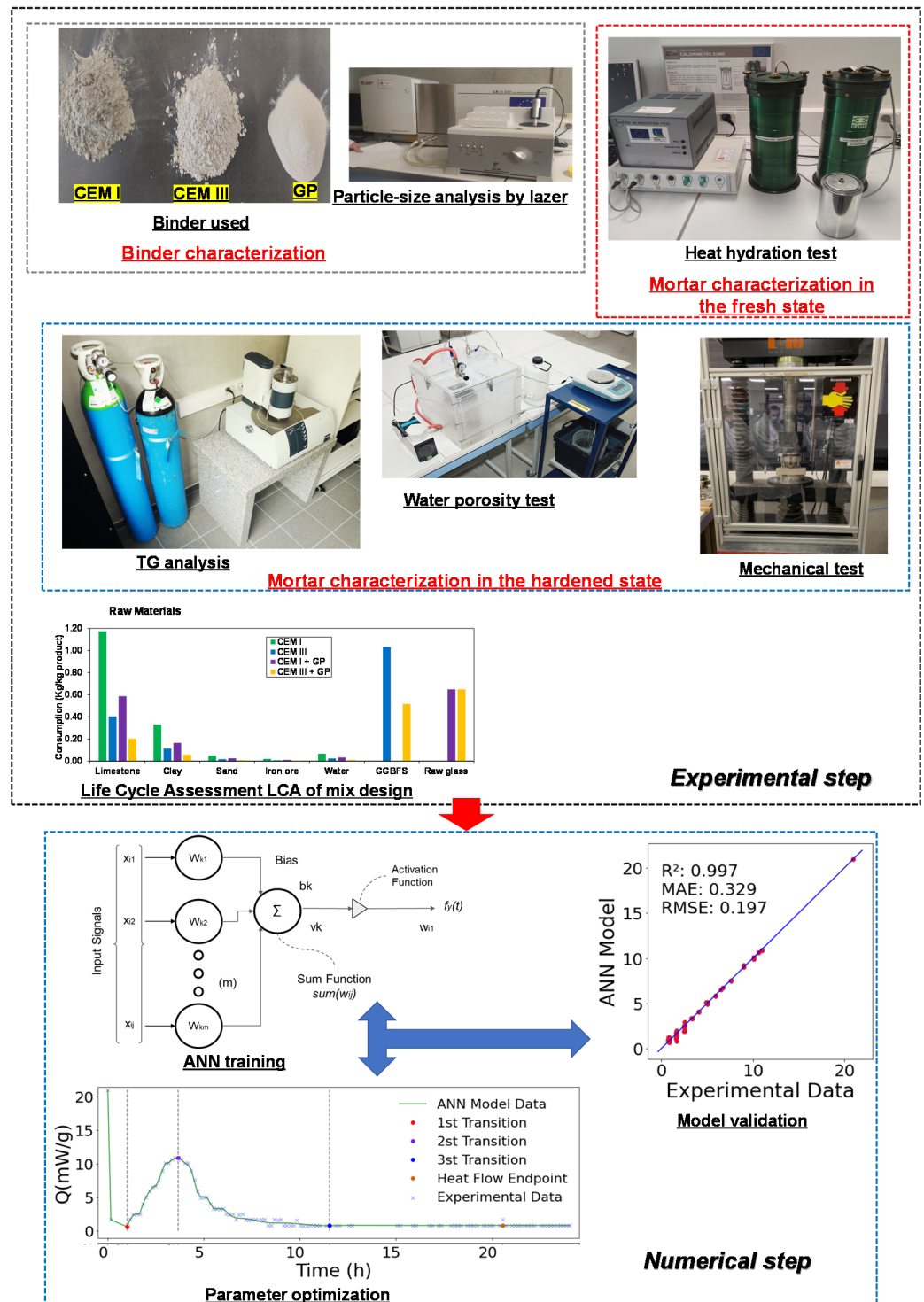


Figure 2. Conceptual study plan.

2.1. Experimental Program

Experiments were carried out to investigate the substitution effect of cement, which is responsible for significant greenhouse gas (GHG) emissions, by other non-biodegradable GHG alternatives, such as glass powder (GP), which represents a significant amount of waste. The use of GP as cement substitution would affect the consistency, the heat of

hydration, and the mechanical properties. In the first step, a characterization of the binders' constituents was performed through particle size analysis and density analysis. Afterward, mortars with Portland cement (CEM I 52.5 N), blast furnace cement (CEM III 32.5 N), and glass powder (GP) were mixed. In this study, 50% of the cement mass was replaced by GP. Indeed, Zeybek et al. [57] conducted a series of compressive strength, splitting tensile strength, and flexural strength tests to investigate the effect of waste glass powder on the mechanical properties of concrete. In their study, glass powder was used to replace up to 50% of cement. The study conducted by Kalakada et al. [58] showed also a decrease in compressive strength at high cement substitution. The compression strength of the concrete specimen was reduced by 65% when 50% of the cement was replaced with glass powder. In this study, it was chosen to replace the cement by 50% of GP in mass in view of other experiences in the literature with high substitution rates, but it is important to notice that focus is given on the proper validation of the relevance of the ANN model with materials having a low hydration heat (which is expected at those high substitution rates—up to 50%). The microstructural characterization of the tested mortars was conducted using an isothermal calorimeter, water porosity, and a TG analysis. In addition, the workability and mechanical strength of the mortars were also assessed and compared to control mortars with CEM I and CEM III. To explain the improvement of the mechanical strength and the decrease in the porosity in the long term, the thermogravimetric analysis was performed after 90 days.

2.1.1. Raw Materials

Two types of cement were used in this study, CEM I 52.5 N and CEM III 32.5 N in compliance with the European standard [59]. Glass powder was used as mass substituents of cement. The glass powder was recovered from glass waste of demolition, provided by the waste disposal plant of Caen's metropolitan region (Normandy, France). The density of binders was determined using a helium pycnometer and the particle size distribution was assessed by a laser particle size analyzer in the wet process in compliance with the European standard [60]. Figure 3 shows the particle size distribution of the used binders. The results show that the studied CEM I and CEM III were almost the same size as the literature result [61] and presented a finer particle size when compared to GP. Indeed, the average particle sizes D_{50} of the investigated binders were 16, 13, and 40 μm for CEM I, CEM III, and GP, respectively, as reported in Table 2. Several studies proved that a GP fineness finer than 75 μm would produce a pozzolanic reaction instead of alkali-silica reaction (ASR) [62,63]. Concerning the density results, CEM I presented a high density of about 3150 kg/m^3 compared to those of CEM III and GP, which were 2880 and 2510 kg/m^3 , respectively.

Table 2. Particles size and density of binders used.

	CEM I	CEM III	GP
d_{10} (μm)	3	1.5	8
d_{50} (μm)	16	13	40
d_{90} (μm)	40	32	80
d_{max} (μm)	300	70	120
Density (kg/m^3)	3150	2880	2510

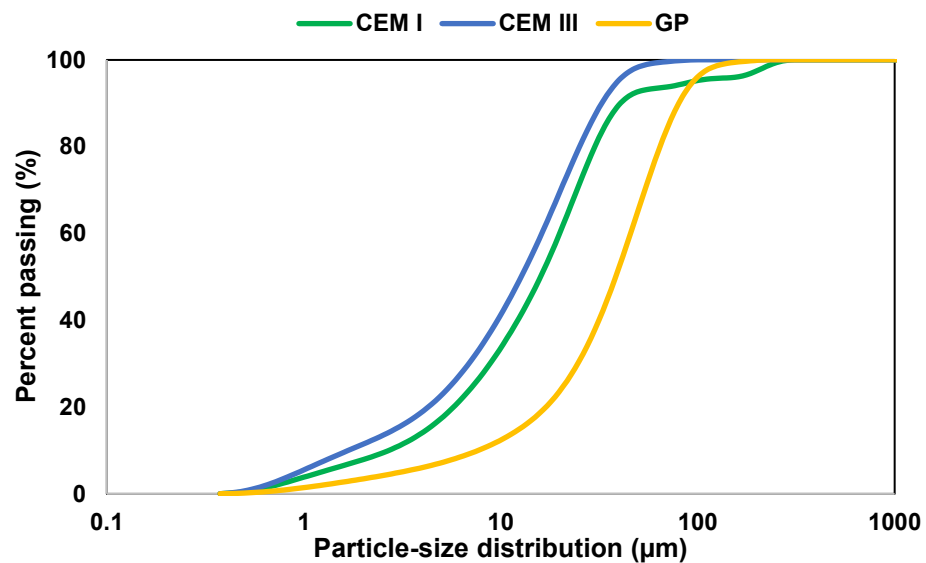


Figure 3. Particle-size distribution of the cements and glass powder used.

2.1.2. Mix Design and Experimental Protocol

The mortar mixture was prepared using the mix design method described by Equations (1)–(4) [64].

$$V_S + V_C + V_{GP} + V_W \approx 1 \text{ m}^3 \quad (1)$$

$$\frac{W}{GP + C} = 0.5 \quad (2)$$

$$\frac{GP}{C + GP} = 0.5 \quad (3)$$

$$\frac{S}{GP + C} = 0.3 \quad (4)$$

where V_S , V_C , V_{GP} , and V_W (m^3) are the sand, cement, glass powder, and water volumes, respectively. S , W , GP , and C (kg) are the sand, effective water, glass powder, and cement contents per cubic meter of mortar, respectively. The water-to-binder ratio was taken as equal to 0.5 (Equation (2)). Such values of paste volume and water-to-binder ratio were chosen to obtain a homogeneous mortar mixture by limiting bleeding and segregation and to ensure its good workability [64]. Moreover, the water-to-binder ratio was chosen high enough to mitigate the phenomenon of self-desiccation due to hydration [65,66]. The cement substitution ratio was fixed at 0.5 (Equation (3)) to maintain the glass powder content (GP) as equal to the cement content (C). The volume of sand (V_S) was fixed to obtain a total mortar volume of 1 m^3 . The mortar mix compositions are given in Table 3. A commercial SikaCem[®] superplasticizer polycarboxylate was added to all the mixtures in order to obtain a better and comparable consistency. Indeed, due to the low content of the superplasticizer, compared to the mortar constituents, its content was neglected. The superplasticizer/cement ratio varied between 0.36% and 0.54%. The slump measured at the fresh state varied between 12 and 21 mm.

In the fresh state, the workability of mortars was assessed using a flow table test according to the ASTM standard [67]. This test is performed by placing mortar in a mini mortar cone, which has been previously wetted, in two layers on a vibrating table. Then, 15 vibrations are applied with a speed of 1 vibration/second. At the end of this test, the flow is measured. In the hardened state, the porosity, and the compressive and the tensile strengths of all specimens were tested. According to the French standard [68], the prismatic mortars of $4 \times 4 \times 16 \text{ cm}^3$ were cast. The specimens were cured at the standard conditions, i.e., for 24 h at $20 \pm 1 \text{ }^\circ\text{C}$ and relative humidity no less than 60%. Then, the specimens were unmolded and cured in water

for different test ages (3, 14, 28, and 90 days) at $(22 \pm 1)^\circ\text{C}$. After that, all mortar specimens were taken out of the water for the mechanical properties tests.

Table 3. Mix proportions of mortar (kg/m^3).

	CEM I	CEM III	CEM I + GP	CEM III + GP
Sand 0/4	1795	1638	1761	1685
CEM I	500	0	250	0
CEM III	0	500	0	250
GP	0	0	250	250
Water	250	250	250	250
Superplasticizer	1.8	1.5	1.4	1.2
Flow (cm)	12	13	17	21

The test of the water porosity consisted of placing the specimens in saturation benches until the total saturation in water, which was ensured by a vacuum pump [69]. Following 24 h of saturation, the specimens were collected, wiped, and their wet and underwater weights measured. After that, the specimens were put in the oven at 105°C for 24 h and a second dry weight measurement was taken. The porosity corresponded to [69].

Concerning the mechanical tests, the corresponding loading rates of the compressive and flexural strength were $2.4 \pm 0.2 \text{ kN/s}$ and $50 \pm 10 \text{ kN/s}$, respectively. Finally, the thermogravimetric analysis (TG) was carried out to monitor the solid phase formations on the mortars and the possible pozzolanic reaction (portlandite—CH, calcite—CC, etc.). The device used was the NETZSCH[®] instrument (STA 449 F5 Jupiter, Selb, Germany). It consists of a sealed chamber to control the atmosphere of the sample by injection of helium gas, an oven to manage the temperature, a weighing module (microbalance), a thermocouple to measure the temperature, and a computer to control and record data. During the test, the temperature should be increased from room temperature to 1200°C with a constant rate of $10^\circ\text{C}/\text{min}$. This velocity is widely used in the literature and it is recommended by the French standard [69]. The obtained TG results were used to calculate the portlandite rate (CH) and the chemically bound water rate (w_b) by Equations (5) and (6) [70].

$$CH\% = \frac{m_{410} - m_{490}}{m_{490}} \times \frac{M_{Ca(OH)_2}}{M_{H_2O}} \times 100\% \quad (5)$$

$$w_b\% = \frac{m_{40} - m_{490}}{m_{490}} \times 100\% \quad (6)$$

where m_{40} , m_{410} , and m_{490} are the sample weights at 40°C , 410°C , and 490°C , respectively. $M_{Ca(OH)_2}$ and M_{H_2O} are the molecular masses of portlandite (CH) and water (H_2O), respectively. To compare the results, CH rate and w_b rate were normalized to 100 g of anhydrous material.

2.2. Data Processing Model

In this section, a binder hydration monitoring method is proposed. This method is based on an artificial neural network (ANN) model processing the data from the hydration heat tracking test. Indeed, a multilayer perceptron regression (MLP) was used to proceed to an initial treatment of the data considered as signals in order to transform them into a time series regression. Afterward, a numerical analysis of the generated model was carried out in order to identify the different transition modes. The identification of the transition modes was based on the local maxima and minima values of the generated model and related to the hydration process.

2.2.1. Artificial Neural Network Modeling

In the literature, the most used data-driven model for building and material behavior is the artificial neural network (ANN) [71–73]. Numerous types of ANNs have been developed over the years with varying characteristics. A multilayer perceptron (MLP) is a class of ANN, which is applied for both classification and regression problems, it is a classical type of neural network, very flexible, and can be used generally to learn a map from inputs to outputs, among other applications. It is classified as supervised learning, using a backpropagation technique for training (cf., Figure 4). All studies in the literature highlight good results in long short-term memory (LSTM) applications showing versatility in a multitude of scenarios [74–77].

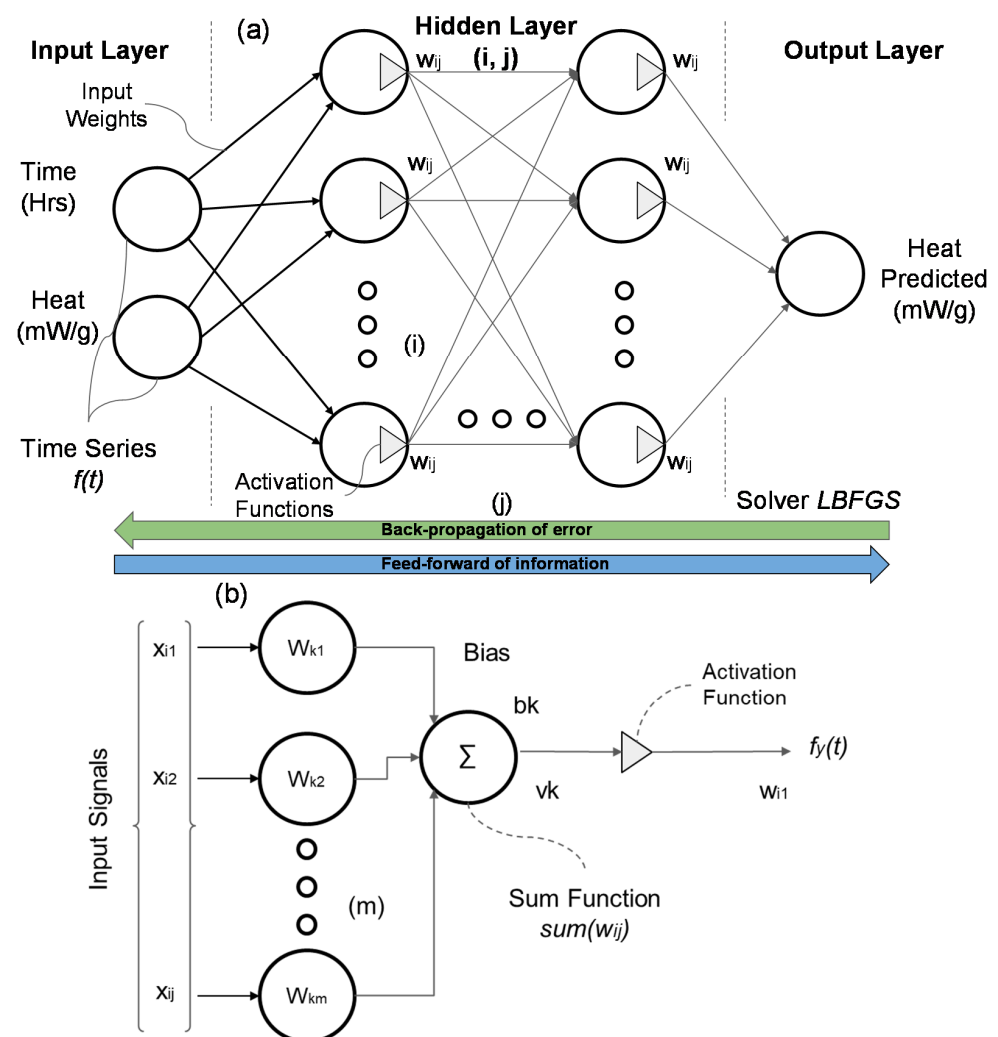


Figure 4. Simplified representation of an artificial neural network and its components: (a) Design Concept of a Multi-Layer Perceptron Model (MLP) and (b) Neuron simplified structure.

The MLP model consists of three parts or nodes organized in the input layer, hidden layers, and output layer. Except for the input nodes, all the other concepts apply non-linear activation functions in which the size of the hidden layer is usually determined by hyperparametric optimization [75]. The details of the inputs and internal weights are optimized depending on the applied problem and dataset.

As seen in Figure 4b, the neuronal structure is also composed of three elements [78,79]: (i) ‘synapses’ or connecting links that are associated with particular weights; (ii) the processing unit that handles the input signals weighted (summing junction) by the synaptic weight and adjusts them by adding a bias value (b_k); (iii) an activation function (φ) that limits

the signal amplitude at the neuron's output. Figure 4b demonstrates a typical neuronal structure, applied for the hidden and output layer. The input layer differs by the absence of the activation function and the single input synapse, connected to the input data. The neuron k can be described mathematically by Equations (7) and (8).

$$u_k = \sum_{j=1}^m x_j \times w_{kj} \quad (7)$$

$$v_k = u_k + b_k \quad (8)$$

where u_k is the linear combiner of the input signal and v_k is the weighted sum of the input values adjusted by the b_k . The activation function is a set of mathematical equations that define the output signal of the neuron k . The activation function may be divided into four distinct groups [80], as in Equations (9)–(12). Equation (9) represents the threshold function, which is equivalent to a Heaviside function. Equation (10) is an identification function (linear function). Equation (11) is a logistic sigmoid function (having a sigmoidal nonlinearity with a as its slope parameter). Equation (12) is a hyperbolic tangent function (another kind of nonlinearity).

$$\varphi(v) = \begin{cases} 1 & \text{if } v > 0 \\ 0 & \text{if } v = 0 \\ -1 & \text{if } v < 0 \end{cases} \quad (9)$$

$$\varphi(V) = 0 \quad (10)$$

$$\varphi(V) = \log f(V) = \frac{1}{1 + e^{-\alpha v}} \quad (11)$$

$$\varphi(V) = \tanh(V) = \frac{2}{1 + e^{-\alpha v}} \quad (12)$$

The sum of the weighted and bias-corrected inputs passes through the activation function φ to obtain the final output signal (y_k), as shown in Equation (13).

$$y_k = \varphi\left(\sum_{j=1}^m x_j \times w_{kj} + b_k\right) \quad (13)$$

The implementation of the ANN model is carried out in three steps. The initial stage is to train the model to minimize the absolute error by altering the weight parameters, based on comparisons between experimental and model outputs, which should be as close as possible. The LBFGS (Limited-Memory Broyden–Fletcher–Goldfarb–Shanno) is a popular optimization algorithm for estimating weight parameters in machine learning. It uses a quasi-Newton method [81–83]. As the original method (LBFGS), it uses an estimate of the inverse Hessian matrix, but in that case, LBFGS stores only some chosen vectors, to be able to represent the model with a required approximation.

2.2.2. Evaluation Metrics

In order to evaluate the final model's performance, the correlation coefficient (R^2), the root mean square error (RMSE), and the mean absolute error (MAE) are employed [84–86]. The aim is to achieve a model that best fits the labeled training data by evaluating all the combined applied metrics. All these metrics are performance indicators commonly used to measure the efficiency of the machine learning models generated. These indicators' definitions are given in Equations (14)–(16), respectively.

$$R^2 = 1 - \frac{\sum_{i=1}^n (y_i - \hat{y}_i)^2}{\sum_{i=1}^n (y_i - \bar{y})^2} \quad (14)$$

$$RMSE = \sqrt{\frac{1}{n} \times \sum_{i=1}^n (\hat{y}_i - y_i)^2} \quad (15)$$

$$MAE = \sum_{i=1}^n \left| \frac{y_i - \hat{y}_i}{y_i} \right| \quad (16)$$

2.2.3. Data Processing/Numerical Model

In addition to the characterization of the microstructure and mechanical properties at several ages, a conceptual framework was built to describe and visualize our study methods after reviewing the relevant current literature [42,44–48]. Each phase is composed of several steps, as explained in detail in the following sections. These main phases are summarized in Figure 5 and as below:

- Collecting data: the experimental data were collected based on heat energy measures within the time, during the cement hydration process. That was the base dataset used in the initial data processing, heat energy within time. Four datasets obtained from CEM I, CEM III, CEM I + GP and CEM III + GP were analyzed. Each dataset contained X data points, in a total of Y datapoints being analyzed;
- Model estimation: concept of the initial data processing, testing, and optimizing all the parameters necessary for the execution of the algorithm, such as MLP hidden layers size, activation functions, and optimization algorithm [71,72,82,85];
- Evaluation of conceived model: based on the mentioned metrics parameters (R^2 , RMSE, MAE), the best parameters setup was evaluated to proceed with the data classification [85,86];
- Mode's identification: based on the generated model data (hydration heat Q vs. time plot), a numerical peak analysis was proceeded to identify the transition zones and, thus, the transition modes of binder hydration with time [42].

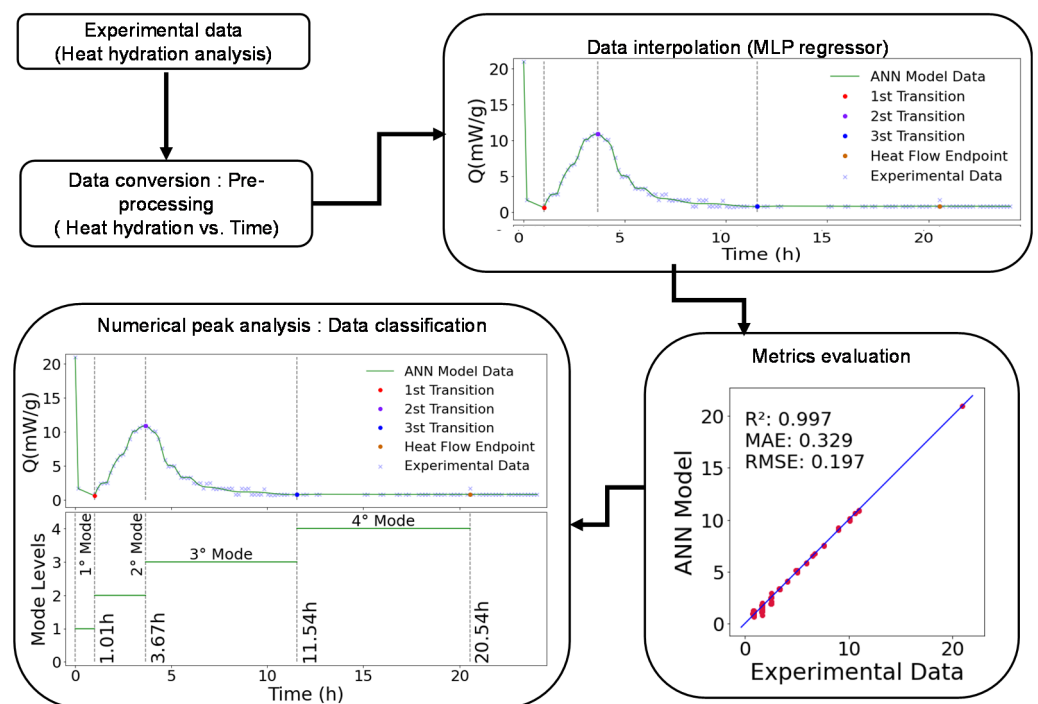


Figure 5. Computational procedure for hydration process classification proposed model.

As a result, the binder hydration modes were obtained, through a staircase levels plot, with respective time transitions [42,45,48]. In addition, within the chemical compositions,

the main difference aspects can be highlighted in the behavior, and the total time of each mode for different samples can be compared.

3. Results and Discussion

3.1. Life Cycle Analysis LCA

Tables 4–6 present the LCA inventory obtained after interpolations and considerations reported in the literature. GGBFS is highlighted by the literature with a potential emission reduction of 78.84% in the production of CEM III [64]. Regarding GP production, its manufacturing process shown in Table 4 is not on an industrial scale according to [65]. For masses, units given are in kg of raw material by kg of produced binder (kg/kg product). For raw materials in volume, such as water, units given are in m³ of raw material by kg of produced binder (m³/kg product). For energy input, it is either given in terms of kWh of energy by kg of produced binder (kWh/kg product) or in kg of utilized fuel source by kg of produced binder (kg/kg product).

Table 4. Cement regulations following European Standard (EN 197-1) [59].

Raw Materials	Units	CEM I (Clinker)	CEM III (GGBFS)	CEM I + GP	CEM III + GP
Limestone	kg/kg product	1.1737	0.4049	0.5868	0.2025
Clay	kg/kg product	0.3307	0.1141	0.1653	0.0570
Sand	kg/kg product	0.0503	0.0174	0.0252	0.0087
Iron ore	kg/kg product	0.0203	0.0070	0.0102	0.0035
Water	m ³ /kg product	0.0668	0.0230	0.0334	0.0115
GGBFS	kg/kg product	-	1.0316	-	0.5158
Raw glass	kg/kg product	-	-	0.6480	0.6480

Table 5. Energy consumption inventory input and calculations.

Energy	Units	CEM I (Clinker)	CEM III (GGBFS)	CEM I + GP	CEM III + GP
Electricity (kWh)	kWh/kg product	0.0687	0.0687	0.0403	0.0403
Petroleum coke	kg/kg product	0.0463	0.0463	0.0231	0.0231
Hard coal	kg/kg product	0.0559	0.0559	0.0280	0.0280
Diesel	kg/kg product	3.04×10^{-7}	3.04×10^{-7}	1.52×10^{-7}	1.52×10^{-7}
Fuel oil	kg/kg product	0.0117	0.0117	0.0058	0.0058
Natural Gas (MJ)	MJ/kg product	0.2777	0.2777	0.8768	0.8768
Light distribution	kg/kg product	0.0043	0.0043	0.0022	0.0022

Table 6. General emissions inventory input and calculations.

Emissions	Units	CEM I (Clinker)	CEM III (GGBFS)	CEM I + GP	CEM III + GP
CO ₂	kg/kg product	0.0687	0.0687	0.0403	0.0403
NO _x	kg/kg product	0.0463	0.0463	0.0231	0.0231
SO ₂	kg/kg product	0.0559	0.0559	0.0280	0.0280
H ₂ O(g)	kg/kg product	3.04×10^{-7}	3.04×10^{-7}	1.52×10^{-7}	1.52×10^{-7}
Particulates	kg/kg product	0.0117	0.0117	0.0058	0.0058
Waste	kg/kg product	0.2777	0.2777	0.8768	0.8768

Figure 6 shows the different raw materials' consumption. The results show a considerable reduction in natural resources replaced by waste. In general, this also implies a reduction in land use, extraction, and other environmental aspects related to the extraction of mineral raw materials using by-products, avoiding dumping and similar impacts.

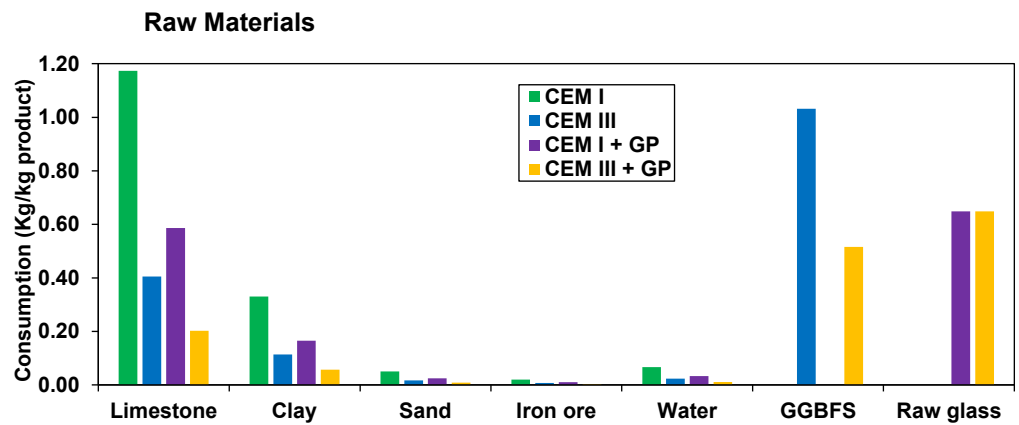


Figure 6. Raw materials’ consumption.

Figure 7 presents the results for the relevant energy demands. Apart from the electricity produced by different renewable resources (hydroelectric, wind, and thermoelectric), all other resources are derived from fossil origins. The fuel that has the greatest impact on clinker production is petroleum coke and hard coal, followed by fuel oil. The proposed formulations with a 50% replacement of cement will contribute to a direct 50% reduction in emissions once the clinker manufacturing process is significantly reduced. Regarding the increase in natural gas consumption, LCA of GP reveals that the results presented are not applied on an industrial scale, while scalability in this area could increase performance by reducing consumption.

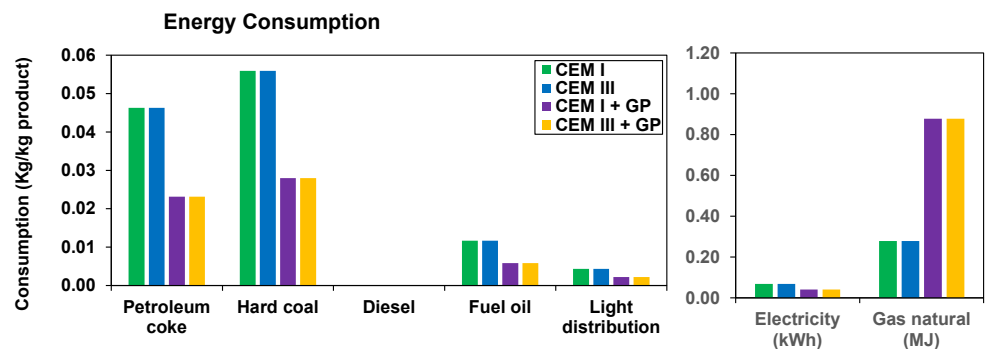


Figure 7. Energy consumption results.

Figure 8 shows the GHG emission results for the formulations studied. The results show a significant reduction in GHG for the formulations containing GP. Regarding mainly CO₂ emissions, CEM III + GP shows a low impact mainly due to the 78.83% reduction of the CEM III formulation and its 50% replacement by GP. Finally, the same reduction profile is observed for the case of heavy metals, i.e., nitrous oxide (NO_x) and sulfur dioxide (SO₂). According to the literature, NO_x is more detrimental to climate change than CO₂, while some authors indicate that it could be 300 times more detrimental to the climate than CO₂.

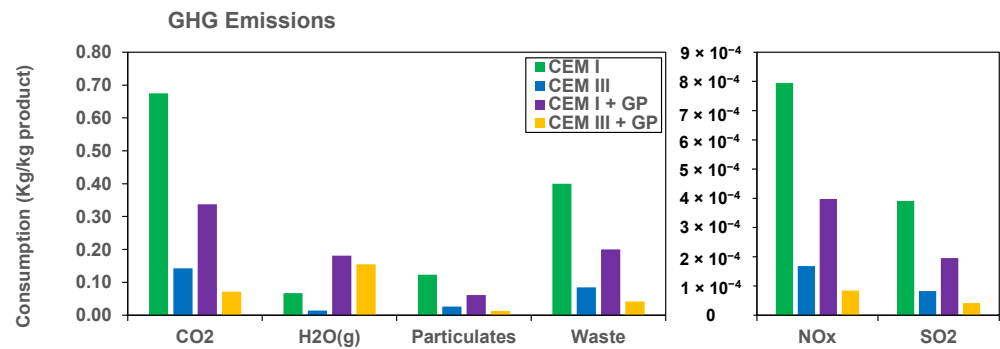


Figure 8. GHG Emissions results.

3.2. Experimental Results

Table 3 presents the flow values measured of the tested mortars. The flow values vary between 12 and 21 mm. Moreover, an improvement in workability is obtained of up to 41.6% and 23.5% for CEM I + GP and CEM III + GP compared to mortars with CEM I and CEM III, respectively. This result is attributed to the higher fineness of GP compared to cement. Therefore, the substitution of cement by GP decreases the water demand for hydration process, i.e., by increasing the amount of free water and workability of the pastes [24].

Figure 9 presents the evolution of the porosity, and the compressive and the tensile strengths (from flexural tests) at several curing ages (3, 14, 28, and 90 days). In general, CEM III presents less water porosity in comparison with CEM I. This phenomenon is explained by the presence of slag in CEM III, which leads to the pores clogging by creating other ranges of non-connected pores [87]. However, after 3 days of curing, the mortars containing GP show high porosity compared to those with only cement. This phenomenon is due to the fineness of GP used, which changes the microstructure and the pore-size distribution [15,24]. A proportional decrease in porosity is observed with increasing age for all mix designs. At 90 days, this decrease is of the order of 4.6%, 2.5%, 12.4%, and 7.9% for mortars based on CEM I, CEM III, CEM I + GP, and CEM III + GP, respectively, compared to the results at 3 days. This result seems to be in good agreement with those found previously by other authors [15,24,49,50].

When it comes to mechanical strength, for all mortars, an increase is observed and this is due to the continuous hydration of the binder with the curing time [22]. In addition, the use of GP with a replacement of 50% of the cement decreases the mechanical strength in the short term. This is due to a dilution effect, which is the immediate consequence of the substitution of a more reactive powder (cement) with a less reactive powder (GP) in the short term [12]. Nevertheless, the mechanical strength does not cease increasing with curing time [15,22,24]. This phenomenon is due to continuous pozzolanic reactions between portlandite ($\text{Ca}(\text{OH})_2$) and silica originating from GP, as highlighted by Idir et al. [55], in addition to the slag present in CEM III, as also demonstrated below by the TG analysis. After 90 days of curing time, the CEM I + GP presents a decrease of about 28% and 17.7% in compressive and tensile strength, respectively, compared to CEM I. For CEM III + GP, the decrease is about 57% and 56% in compressive and tensile strength, respectively, compared to CEM III. These results are in agreement with those reported by Adesina et al. [88]. Nevertheless, these values are adequate for the use of CEM I + GP in the construction sector and particularly in prefabricated structural elements.

Porosity (%)				
CEM I	19.4	19.2	19.1	18.5
CEM III	16.1	15.8	15.7	15.7
CEM I + GP	24.9	24.5	24.3	21.8
CEM III + GP	31.7	31.2	29.5	29.2
	3d	14d	28d	90d

Compressive strength (MPa)				
CEM I	12.1	28.3	43.6	46.5
CEM III	8.7	19.2	25.7	35.1
CEM I + GP	10.1	16.5	27.4	33.5
CEM III + GP	4.3	8.2	10.6	15.1
	3d	14d	28d	90d

Tensile strength (MPa)				
CEM I	5.6	5.9	7.2	7.9
CEM III	5.2	5.1	6.8	7.1
CEM I + GP	3.5	3.6	3.9	6.5
CEM III + GP	1.5	1.2	2.8	3.1
	3d	14d	28d	90d

Figure 9. Porosity, and compressive and tensile strengths of mortars used.

To investigate the pozzolanic reaction of GP with portlandite (CH), a thermogravimetric (TG) analysis is conducted at 90 days. Figure 10 shows the three main phases formed in mortars with CEM I and CEM III. The mortar with CEM III has less portlandite and calcite (CC) amounts than CEM I mortar does. This is due to the activated pozzolanic reaction of the blast furnace slag present in the CEM III cement. Nevertheless, in the case of mortars with GP, the two peaks related to portlandite and calcite are reduced, showing the consumption of CH by GP to produce additional CSH hydrates [24]. An increase in the first peak is observed. Indeed, the three phases correspond generally to three processes according to [89,90]. The first band below 200 °C is due to the loss of free water as well as the dehydration of calcium silicate hydrate (CSH), ettringite (A_{Ft}), calcium monosulfaluminate, hemicarboaluminate, or calcium monocarboaluminate (all these material phases are denoted as A_{Fm}). The second peak around 400–500 °C is contributed to the dehydroxylation of portlandite (CH), while the decarbonization of calcium carbonates (CC) takes place at 700–800 °C. From dTG patterns, the A_{Ft} and A_{Fm} material phases are difficult to dissociate, as the corresponding bands are large, and the decomposition temperatures of these phases are very narrow and overlay each other.

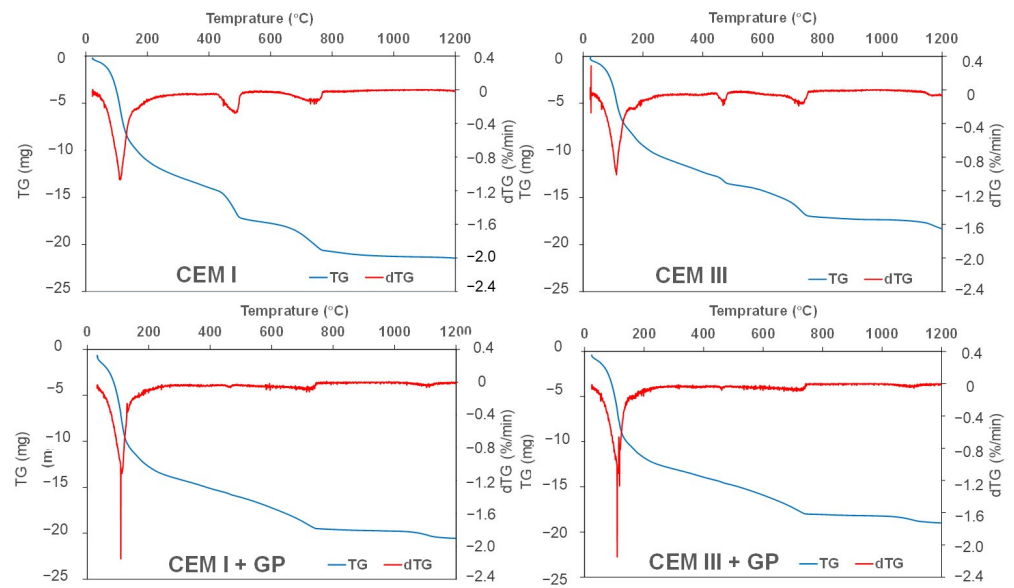


Figure 10. TG and dTG curves of the studied mortars.

Based on TG results, the normalized amounts of the bound water (w_b) and portlandite (CH) are both presented in Figure 11. Indeed, the w_b rate indicates the volume of reaction products (including CSH, A_{Ft} , A_{Fm} , and CH) formed during cement hydration, while normalized CH can be interpreted as an indication of changes in the assemblage of reaction products (CH consumption due to the formation of additional CSH hydrates) as highlighted by Damidot et al. [91]. Figure 11 shows that for the mortars containing low clinker content, the w_b rate is lower than for the standard mortar (CEM I).

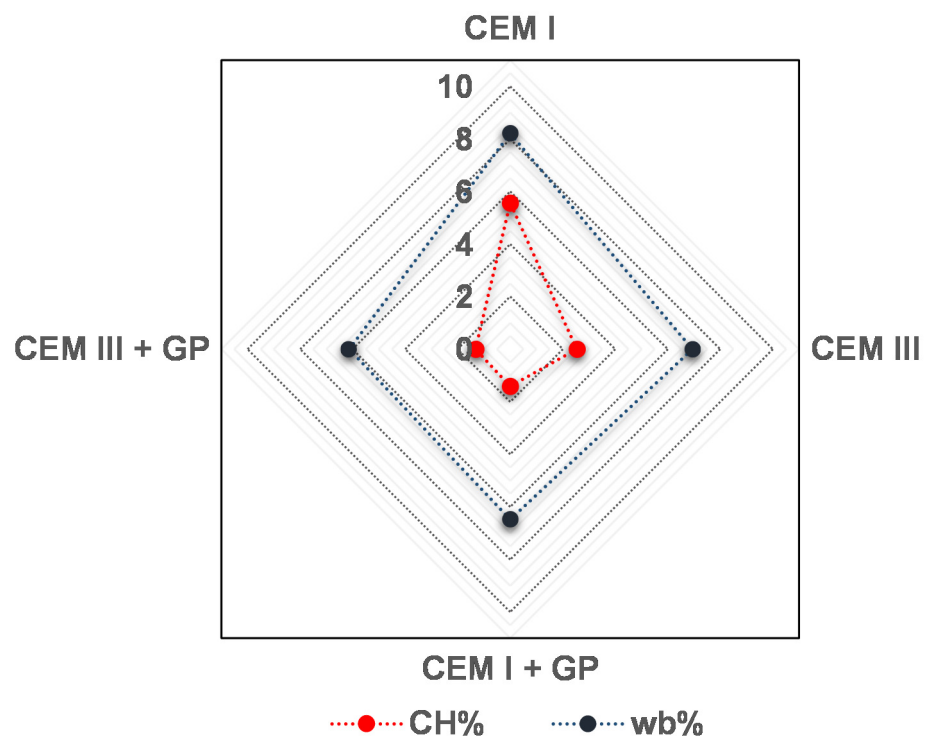


Figure 11. CH% and w_b % of mortars studied.

The increase in w_b in the mortars with GP is related to pozzolanic reactions. Indeed, silica reacts chemically with calcium hydroxide (CH) and produces additional CSH phases.

Due to CH consumption, the normalized CH value for mortar with GP is lower than that for the standard mortars (CEM I and CEM III). These data show the same trend as those reported in literature [92,93], where w_b and CH values for both pure and blended pastes with silica fume were estimated and measured.

3.3. Data Processing/Numerical Results

Figure 12 shows the experimental data and those predicted by the ANN model for the heat of hydration in mW/g. Indeed, the models translating the hydration behavior of CEM I, CEM I + GP, CEM III, and CEM III + GP mortars provide a good agreement with the data found experimentally with a difference of relevance more important for the MAE and RMSE metrics. For the RMSE, the lowest results are obtained with the CEM III + GP results with a 0.92 R^2 score, with the further metrics appointed in the same evaluation for near 0.35 for MAE, and with an improvement for the RMSE, at a value of 0.20, the best result for all datasets.

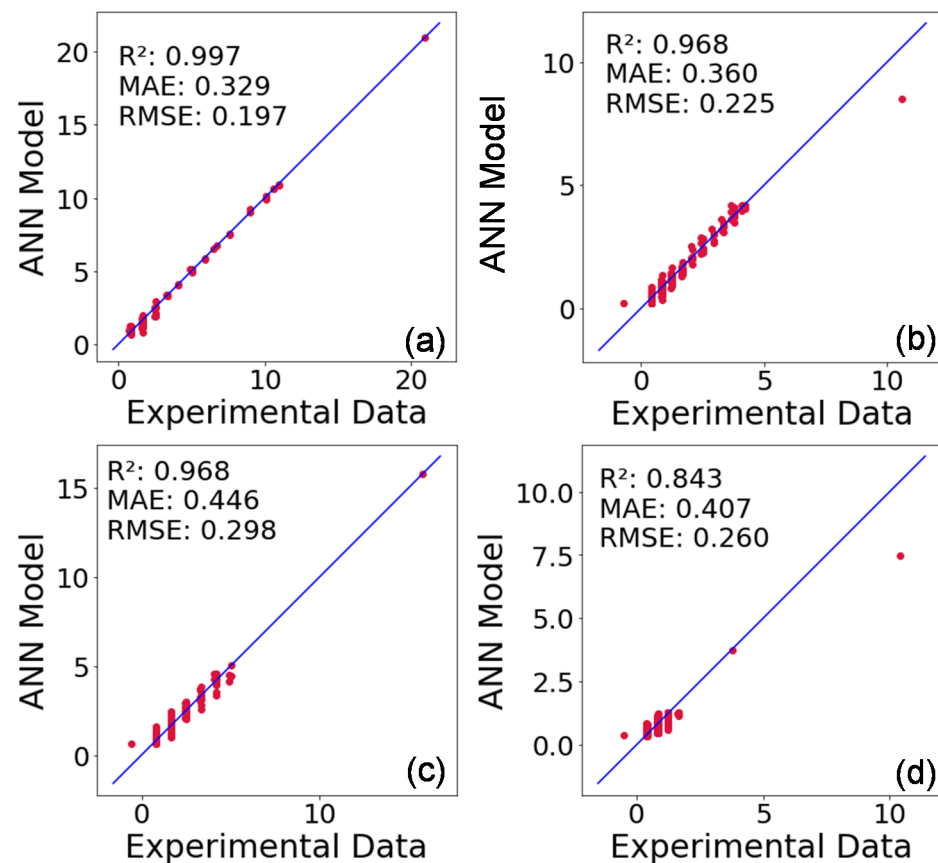


Figure 12. ANN models versus experimental data (for the heat of hydration in mW/g) with error metrics for (a) CEM I, (b) CEM I + GP, (c) CEM III, and (d) CEM III + GP.

The hydration modes identification of CEM I, CEM I + GP, CEM III, and CEM III + GP are shown in Figure 13a,b and Figure 14a,b, respectively. In general, the proposed model identifies four main modes [32], including the initial reaction and slow reaction period (Mode 1), acceleration period (Mode 2), deceleration period (Mode 3), and stability period (Mode 4) in the history of heat flow. As shown in Figures 13 and 14, the standard mortar with CEM I started an earlier acceleration period than the other mortars studied with a higher heat release. This mode corresponds to the induction phenomenon interpreted by the geochemistry dissolution theory that the primary mechanism controlling the kinetics up to the end of the induction period is the undersaturation of this surface layer [94]. In addition, tri-calcium aluminat (C_3A) reacts promptly with water from an early age to form

calcium hydroaluminate ($3\text{CaO}-\text{Al}_2\text{O}_3-\text{Ca}(\text{OH})_2-n\text{H}_2\text{O}$ or hydroxy- A_{Fm}), as mentioned by Nguyen et al. [32].

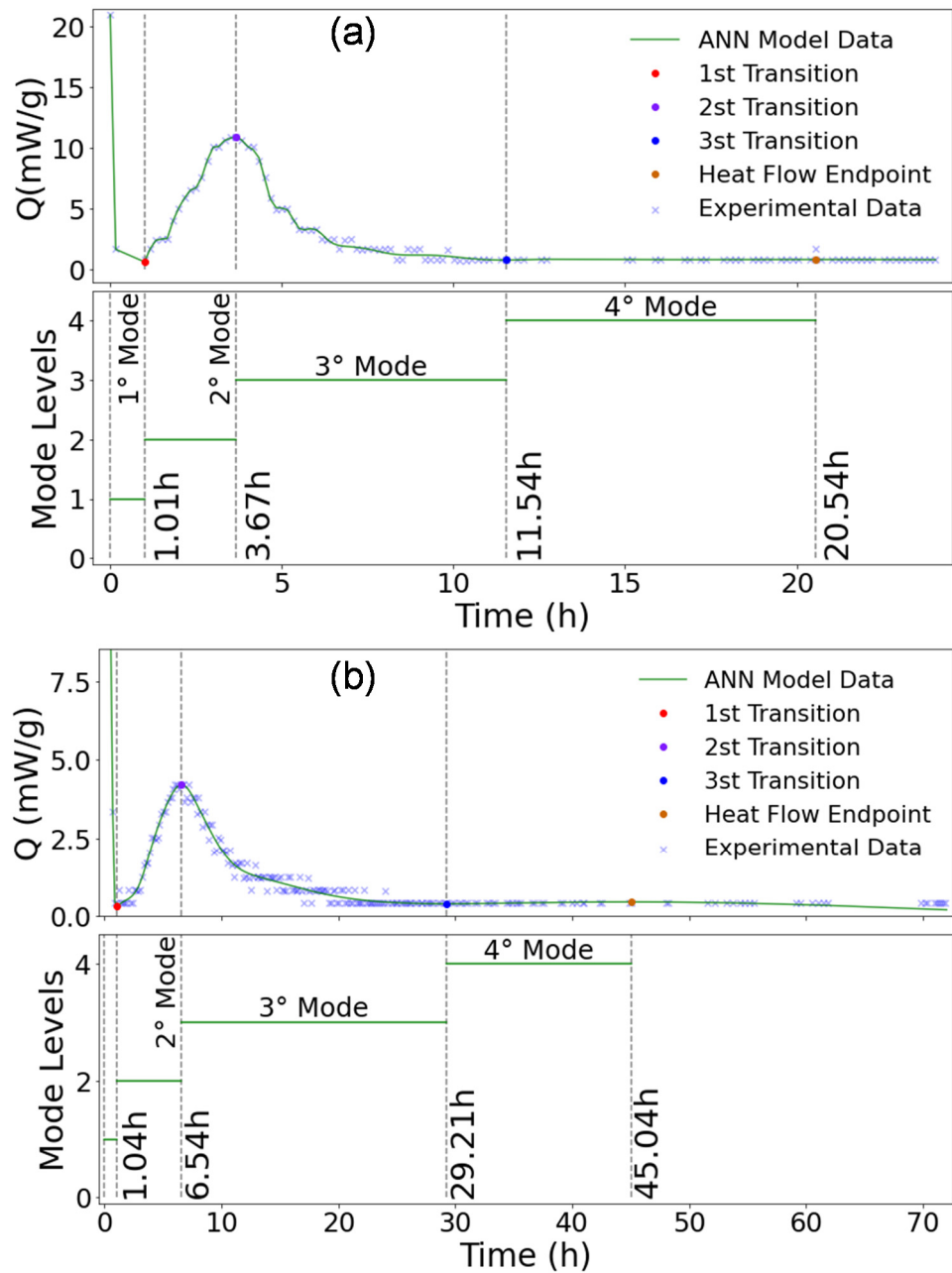


Figure 13. Heat of hydration, ANN model generated, modes, and transitions identification: (a) CEM I and (b) CEM I + GP.

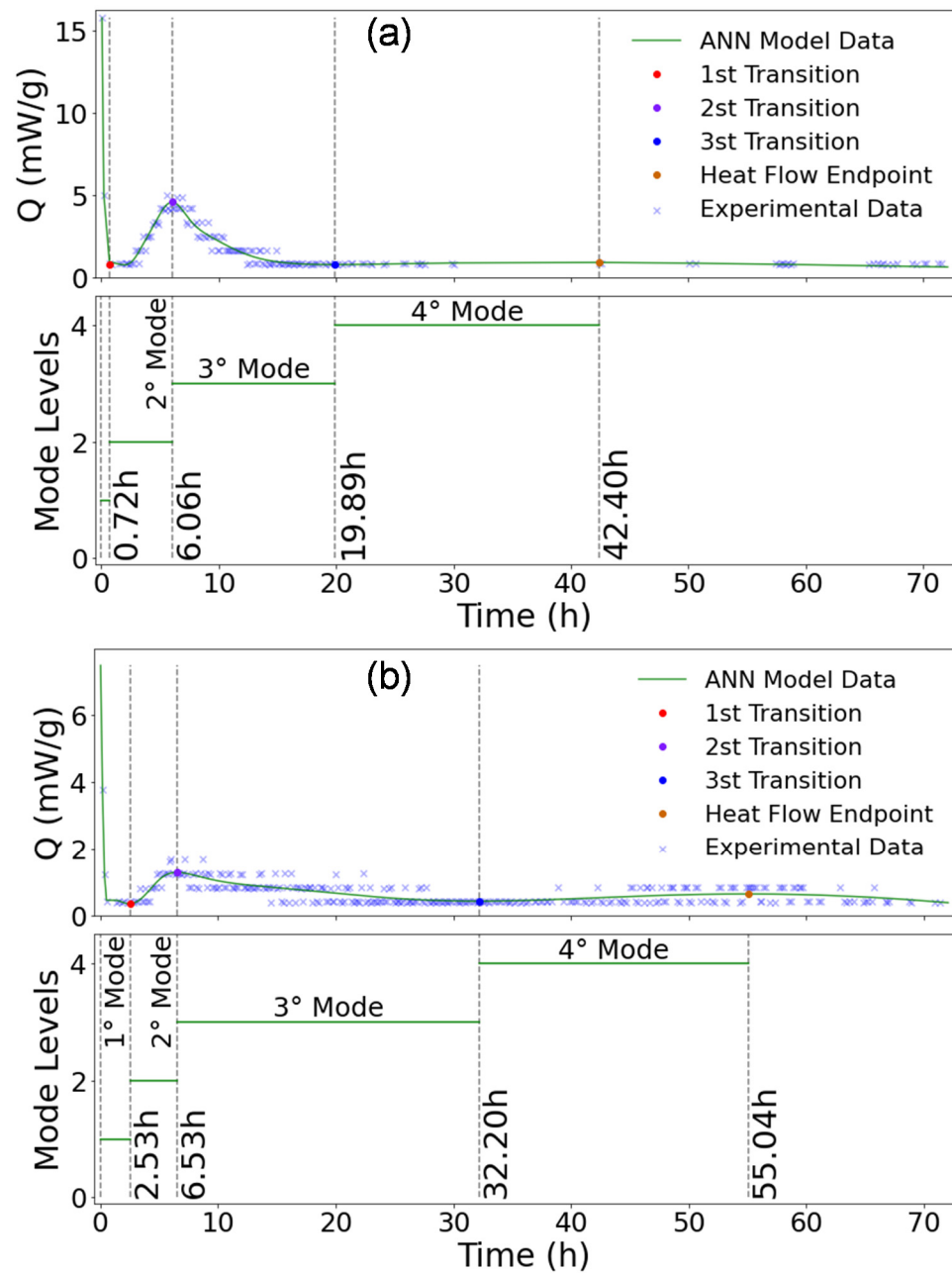


Figure 14. Heat of hydration, ANN model generated, modes, and transitions identification: (a) CEM III and (b) CEM III + GP.

As shown in Figures 13b and 14a, CEP I + GP and CEM III mortars present almost the same behavior in term of peaks position. Nevertheless, these peaks start at 6.78 h and 7.58 h from the first water contact of the binder for the CEM III and CEM I + GP mortars, respectively. This time delay can be explained by the fact that the containing slag in the CEM III is more reactive than the glass powder.

In the second mode, the peak value decreases and shifts toward a longer hydration time when the CEM III and GP are used. This phenomenon could be attributed to the consumption of C_3S (Alite), which is consistent with the hydration heat rate. It is known that the hydration rate of C_3S is much higher than that of C_2S (Belite) due to the higher solubility and lower activation energy of C_3S compared to C_2S [95]. Indeed, the solubility of C_3S is between 5 and 8 times higher than that of C_2S [95]. Therefore, it could be concluded that Mode 2 is strongly affected by the hydration of C_3S , and this state is in good agreement with the literature [96]. At the end of the induction period, CSH and Portlandite (CH) begin

to develop fast. There is still considerable controversy about the trigger for this increase in reaction rate. Indeed, in pastes, it seems that the CH precipitation is the trigger.

Mode 3 corresponds to the renewed dissolution of C_3A with the formation of ettringite (A_{Ft}). Due to this retardation of the C_3A reaction with sulfate, the main reaction of this phase should occur after the main peak of the reaction of alite in a properly sulfated Portland cement. However, in CEM I, the formation of ettringite continues after the exhaustion of sulfate in the solution [97]. In conclusion, the ANN model makes it possible to determine when the initial hydration phase is completed, i.e., after 20.54 h, 42.40 h, 45.04 h, and 55.04 h for mortar based on CEM I, CEM III, CEM I + GP, and CEM III + GP, respectively.

4. Conclusions

An ANN model is used for the first time to identify the different hydration modes of binders using only the heat hydration test as an input parameter. The method is based on a MLP regressor that maps the input signal and generates a fitted model. Afterward, a numerical approach is proceeded to identify the different hydration modes with respective times.

Indeed, ANN model detects four modes during the hydration process. In addition, the model proposed provides similar results in terms of heat of hydration in comparison to the experimental results with $R^2 = 0.997, 0.968, 0.968, \text{ and } 0.921$ for CEM I, CEM III, CEM I + GP, and CEM III + GP, respectively. In addition to the mechanical strength achieved, the replacement of 50% of cement by GP is significantly positive for the LCA results. Indeed, the GHG emissions present the most significant results, by reducing 50% and 80% of the emissions of CO_2 and $NO_x + SO_2$ for the CEM I + GP and CEM III + GP mixtures, respectively.

It is revealed in this study that waste glass can be employed as a partial cement substitute in mortar and would be beneficial for GHG emissions of concrete. The present study identifies waste glass as suitable, accessible in large quantities, a local eco-material, and suitable for concrete construction from an economic and environmental standpoint. Nevertheless, when waste glass is employed as partial replacement for cement, the strength values are reduced, which needs to be investigated in the lab for proper mix design and use of the materials. To address this shortcoming, future research will focus on combining waste glass with other recycling fibers. Moreover, the proposed ANN model allows cement manufacturers to quickly identify the different hydration modes of new binders by using only the heat hydration test as an input parameter.

Author Contributions: Conceptualization, investigation, data curation, writing—original draft preparation, methodology, F.B., D.L.L.T., M.H.B. and Y.E.M.; software, D.L.L.T.; validation, formal analysis, writing—review and editing, visualization, supervision, resources, L.F.d.A.L.B. and Y.E.M. All authors have read and agreed to the published version of the manuscript.

Funding: This research was funded by the European Regional Development Fund for having sponsored this study in the frame of a BLUEPRINT to a Circular Economy project (Interreg V A France (Channel) England, Project n°206).

Institutional Review Board Statement: Not applicable.

Informed Consent Statement: Not applicable.

Data Availability Statement: The experimental and computational data presented in the present paper are available from the corresponding author upon request.

Acknowledgments: Authors thank the European Regional Development Fund for financing the research through the BLUEPRINT project.

Conflicts of Interest: The authors declare no conflict of interest.

References

1. Miller, S.A.; Horvath, A.; Monteiro, P.J.M. Readily Implementable Techniques Can Cut Annual CO₂ Emissions from the Production of Concrete by over 20%. *Environ. Res. Lett.* **2016**, *11*, 074029. [CrossRef]
2. Gencil, O.; Karadag, O.; Oren, O.H.; Bilir, T. Steel Slag and Its Applications in Cement and Concrete Technology: A Review. *Constr. Build. Mater.* **2021**, *283*, 122783. [CrossRef]
3. Prakash, R.; Thenmozhi, R.; Raman, S.N.; Subramanian, C. Characterization of Eco-friendly Steel Fiber-reinforced Concrete Containing Waste Coconut Shell as Coarse Aggregates and Fly Ash as Partial Cement Replacement. *Struct. Concr.* **2020**, *21*, 437–447. [CrossRef]
4. Sundaresan, S.; Ramamurthy, V.; Meyappan, N. Improving Mechanical and Durability Properties of Hypo Sludge Concrete with Basalt Fibres and SBR Latex. *Adv. Concr. Constr.* **2021**, *12*, 327–337. [CrossRef]
5. WBCSD World Business Council for Sustainable Development and International Energy Agency Cement Technology Roadmap 2009: Carbon Emissions Reductions up to 2050. Available online: <https://www.iea.org/reports/cement-technology-roadmap-carbon-emissions-reductions-up-to-2050> (accessed on 11 November 2022).
6. Shen, D.; Jiao, Y.; Kang, J.; Feng, Z.; Shen, Y. Influence of Ground Granulated Blast Furnace Slag on Early-Age Cracking Potential of Internally Cured High Performance Concrete. *Constr. Build. Mater.* **2020**, *233*, 117083. [CrossRef]
7. Antoni; Chandra, L.; Hardjito, D. The Impact of Using Fly Ash, Silica Fume and Calcium Carbonate on the Workability and Compressive Strength of Mortar. *Procedia Eng.* **2015**, *125*, 773–779. [CrossRef]
8. Bani Ardalan, R.; Joshaghani, A.; Hooton, R.D. Workability Retention and Compressive Strength of Self-Compacting Concrete Incorporating Pumice Powder and Silica Fume. *Constr. Build. Mater.* **2017**, *134*, 116–122. [CrossRef]
9. Chandra Paul, S.; Šavija, B.; Babafemi, A.J. A Comprehensive Review on Mechanical and Durability Properties of Cement-Based Materials Containing Waste Recycled Glass. *J. Clean. Prod.* **2018**, *198*, 891–906. [CrossRef]
10. Serpa, D.; Santos Silva, A.; de Brito, J.; Pontes, J.; Soares, D. ASR of Mortars Containing Glass. *Constr. Build. Mater.* **2013**, *47*, 489–495. [CrossRef]
11. Shayan, A.; Xu, A. Value-Added Utilisation of Waste Glass in Concrete. *Cem. Concr. Res.* **2004**, *34*, 81–89. [CrossRef]
12. Zidol, A.; Tognonvi, M.T.; Tagnit-Hamou, A. Effect of Glass Powder on Concrete Sustainability. *New J. Glas. Ceram.* **2017**, *7*, 34–47. [CrossRef]
13. Shi, C.; Zheng, K. A Review on the Use of Waste Glasses in the Production of Cement and Concrete. *Resour. Conserv. Recycl.* **2007**, *52*, 234–247. [CrossRef]
14. Ling, T.-C.; Poon, C.-S.; Wong, H.-W. Management and Recycling of Waste Glass in Concrete Products: Current Situations in Hong Kong. *Resour. Conserv. Recycl.* **2013**, *70*, 25–31. [CrossRef]
15. Bouchikhi, A.; Benzerzour, M.; Abriak, N.-E.; Maherzi, W.; Mamindy-Pajany, Y. Study of the Impact of Waste Glasses Types on Pozzolanic Activity of Cementitious Matrix. *Constr. Build. Mater.* **2019**, *197*, 626–640. [CrossRef]
16. Du, Y.; Yang, W.; Ge, Y.; Wang, S.; Liu, P. Thermal Conductivity of Cement Paste Containing Waste Glass Powder, Metakaolin and Limestone Filler as Supplementary Cementitious Material. *J. Clean. Prod.* **2021**, *287*, 125018. [CrossRef]
17. Yin, W.; Li, X.; Sun, T.; Chen, Y.; Xu, F.; Yan, G.; Xu, M.; Tian, K. Utilization of Waste Glass Powder as Partial Replacement of Cement for the Cementitious Grouts with Superplasticizer and Viscosity Modifying Agent Binary Mixtures: Rheological and Mechanical Performances. *Constr. Build. Mater.* **2021**, *286*, 122953. [CrossRef]
18. Szudek, W.; Gołek, Ł.; Malata, G.; Pytel, Z. Influence of Waste Glass Powder Addition on the Microstructure and Mechanical Properties of Autoclaved Building Materials. *Materials* **2022**, *15*, 434. [CrossRef]
19. Gołek, Ł.; Szudek, W.; Bładek, M.; Cięciwa, M. The Influence of Ground Waste Glass Cullet Addition on the Compressive Strength and Microstructure of Portland Cement Pastes and Mortars | Wpływ Dodatku Mielonej Słuczki Szklanej Na Wytrzymałość Orz Mikrostrukturę Zaczynów i Zapraw z Cementu Portlandzki. *Cem. Wapno Bet.* **2020**, *2020*, 480–494. [CrossRef]
20. Szydłowski, J.; Szudek, W.; Gołek, Ł. Effect of Temperature on the Long-Term Properties of Mortars Containing Waste Glass Powder and Ground Granulated Blast Furnace Slag. *Cem. Wapno Bet.* **2021**, *26*, 264–278. [CrossRef]
21. Gołek, Ł. Glass Powder and High-Calcium Fly Ash Based Binders—Long Term Examinations. *J. Clean. Prod.* **2019**, *220*, 493–506. [CrossRef]
22. Gołek, Ł. New Insights into the Use of Glass Cullet in Cement Composites—Long Term Examinations. *Cem. Concr. Compos.* **2022**, *133*, 104673. [CrossRef]
23. de Castro, S.; de Brito, J. Evaluation of the Durability of Concrete Made with Crushed Glass Aggregates. *J. Clean. Prod.* **2013**, *41*, 7–14. [CrossRef]
24. Boukhelf, F.; Cherif, R.; Trabelsi, A.; Belarbi, R.; Bachir Bouiadjra, M. On the Hygrothermal Behavior of Concrete Containing Glass Powder and Silica Fume. *J. Clean. Prod.* **2021**, *318*, 128647. [CrossRef]
25. Chand, G.; Happy, S.K.; Ram, S. Assessment of the Properties of Sustainable Concrete Produced from Quaternary Blend of Portland Cement, Glass Powder, Metakaolin and Silica Fume. *Clean. Eng. Technol.* **2021**, *4*, 100179. [CrossRef]
26. Boesch, M.E.; Vadenbo, C.; Saner, D.; Huter, C.; Hellweg, S. An LCA Model for Waste Incineration Enhanced with New Technologies for Metal Recovery and Application to the Case of Switzerland. *Waste Manag.* **2014**, *34*, 378–389. [CrossRef]
27. Sánchez, A.R.; Ramos, V.C.; Polo, M.S.; Ramón, M.V.L.; Utrilla, J.R. Life Cycle Assessment of Cement Production with Marble Waste Sludges. *Int. J. Environ. Res. Public Health* **2021**, *18*, 10968. [CrossRef] [PubMed]
28. Valderrama, C.; Granados, R.; Cortina, J.L.; Gasol, C.M.; Guillem, M.; Josa, A. Implementation of Best Available Techniques in Cement Manufacturing: A Life-Cycle Assessment Study. *J. Clean. Prod.* **2012**, *25*, 60–67. [CrossRef]

29. Chen, C.; Habert, G.; Bouzidi, Y.; Jullien, A. Environmental Impact of Cement Production: Detail of the Different Processes and Cement Plant Variability Evaluation. *J. Clean. Prod.* **2010**, *18*, 478–485. [\[CrossRef\]](#)
30. Huntzinger, D.N.; Eatmon, T.D. A Life-Cycle Assessment of Portland Cement Manufacturing: Comparing the Traditional Process with Alternative Technologies. *J. Clean. Prod.* **2009**, *17*, 668–675. [\[CrossRef\]](#)
31. Crossin, E. The Greenhouse Gas Implications of Using Ground Granulated Blast Furnace Slag as a Cement Substitute. *J. Clean. Prod.* **2015**, *95*, 101–108. [\[CrossRef\]](#)
32. Guignone, G.; Calmon, J.; Vieira, G.; Zulcão, R.; Rebello, T. Life Cycle Assessment of Waste Glass Powder Incorporation on Concrete: A Bridge Retrofit Study Case. *Appl. Sci.* **2022**, *12*, 3353. [\[CrossRef\]](#)
33. Zulkarnain, I.; Lai, L.S.; Syakir, M.I.; Rahman, A.A.; Yusuff, S.; Hanafiah, M.M. Life Cycle Assessment of Crushed Glass Abrasive Manufacturing from Recycled Glass. *IOP Conf. Ser. Earth Environ. Sci.* **2021**, *880*, 012054. [\[CrossRef\]](#)
34. Qin, C.; Gong, J.; Xie, G. Modeling Hydration Kinetics of the Portland-Cement-Based Cementitious Systems with Mortar Blends by Non-Assumptive Projection Pursuit Regression. *Thermochim. Acta* **2021**, *705*, 179035. [\[CrossRef\]](#)
35. Tahersima, M.; Tikalsky, P. Finite Element Modeling of Hydration Heat in a Concrete Slab-on-Grade Floor with Limestone Blended Cement. *Constr. Build. Mater.* **2017**, *154*, 44–50. [\[CrossRef\]](#)
36. Kondo, R. Kinetics and Mechanism of the Hydration of Cements. In Proceedings of the Fifth International Symposium on the Chemistry of Cement, Tokyo, Japan, 7–11 October 1968; pp. 203–248.
37. Pommersheim, J.M.; Clifton, J.R. Mathematical Modeling of Tricalcium Silicate Hydration. *Cem. Concr. Res.* **1979**, *9*, 765–770. [\[CrossRef\]](#)
38. Pommersheim, J.M.; Clifton, J.R. Mathematical Modeling of Tricalcium Silicate Hydration. II. Hydration Sub-Models and the Effect of Model Parameters. *Cem. Concr. Res.* **1982**, *12*, 765–772. [\[CrossRef\]](#)
39. He, J.; Long, G.; Ma, K.; Xie, Y.; Ma, C. Hydration Heat Evolution of Portland Cement Paste during Unsteady Steam Curing Process: Modelling and Optimization. *Thermochim. Acta* **2020**, *694*, 178784. [\[CrossRef\]](#)
40. Nguyen, V.T.; Lee, S.Y.; Chung, S.-Y.; Moon, J.-H.; Kim, D.J. Effects of Cement Particle Distribution on the Hydration Process of Cement Paste in Three-Dimensional Computer Simulation. *Constr. Build. Mater.* **2021**, *311*, 125322. [\[CrossRef\]](#)
41. Chu, D.C.; Kleib, J.; Amar, M.; Benzerzour, M.; Abriak, N.-E. Recycling of Dredged Sediment as a Raw Material for the Manufacture of Portland Cement—Numerical Modeling of the Hydration of Synthesized Cement Using the CEMHYD3D Code. *J. Build. Eng.* **2022**, *48*, 103871. [\[CrossRef\]](#)
42. Zhao, Y.; Gao, J.; Chen, G.; Li, S.; Luo, X.; Xu, Z.; Guo, Z.; Du, H. Early-Age Hydration Characteristics and Kinetics Model of Blended Cement Containing Waste Clay Brick and Slag. *J. Build. Eng.* **2022**, *51*, 104360. [\[CrossRef\]](#)
43. Krstulović, R.; Dabić, P. A Conceptual Model of the Cement Hydration Process. *Cem. Concr. Res.* **2000**, *30*, 693–698. [\[CrossRef\]](#)
44. Dabić, P.; Krstulović, R.; Rušić, D. A New Approach in Mathematical Modelling of Cement Hydration Development. *Cem. Concr. Res.* **2000**, *30*, 1017–1021. [\[CrossRef\]](#)
45. Xu, Z.; Shen, J.; Qu, Y.; Chen, H.; Zhou, X.; Hong, H.; Sun, H.; Lin, H.; Deng, W.; Wu, F. Using Simple and Easy Water Quality Parameters to Predict Trihalomethane Occurrence in Tap Water. *Chemosphere* **2022**, *286*, 131586. [\[CrossRef\]](#)
46. Hong, H.; Zhang, Z.; Guo, A.; Shen, L.; Sun, H.; Liang, Y.; Wu, F.; Lin, H. Radial Basis Function Artificial Neural Network (RBF ANN) as Well as the Hybrid Method of RBF ANN and Grey Relational Analysis Able to Well Predict Trihalomethanes Levels in Tap Water. *J. Hydrol.* **2020**, *591*, 125574. [\[CrossRef\]](#)
47. Lin, H.; Dai, Q.; Zheng, L.; Hong, H.; Deng, W.; Wu, F. Radial Basis Function Artificial Neural Network Able to Accurately Predict Disinfection By-Product Levels in Tap Water: Taking Haloacetic Acids as a Case Study. *Chemosphere* **2020**, *248*, 125999. [\[CrossRef\]](#)
48. Chen, Y.; Yu, G.; Long, Y.; Teng, J.; You, X.; Liao, B.-Q.; Lin, H. Application of Radial Basis Function Artificial Neural Network to Quantify Interfacial Energies Related to Membrane Fouling in a Membrane Bioreactor. *Bioresour. Technol.* **2019**, *293*, 122103. [\[CrossRef\]](#)
49. Cook, R.; Han, T.; Childers, A.; Ryckman, C.; Khayat, K.; Ma, H.; Huang, J.; Kumar, A. Machine Learning for High-Fidelity Prediction of Cement Hydration Kinetics in Blended Systems. *Mater. Des.* **2021**, *208*, 109920. [\[CrossRef\]](#)
50. Subasi, A.; Yilmaz, A.S.; Binici, H. Prediction of Early Heat of Hydration of Plain and Blended Cements Using Neuro-Fuzzy Modelling Techniques. *Expert Syst. Appl.* **2009**, *36*, 4940–4950. [\[CrossRef\]](#)
51. Salleh, M.N.M.; Talpur, N.; Kashif, H. Adaptive Neuro-Fuzzy Inference System: Overview, Strengths, Limitations, and Solutions. In Proceedings of the International Conference on Data Mining and Big Data, Fukuoka, Japan, 27 July–1 August 2017; pp. 527–535.
52. Luo, D.; Wei, J. Hydration Kinetics and Phase Evolution of Portland Cement Composites Containing Sodium-Montmorillonite Functionalized with a Non-Ionic Surfactant. *Constr. Build. Mater.* **2022**, *333*, 127386. [\[CrossRef\]](#)
53. Riding, K.A.; Poole, J.L.; Folliard, K.J.; Juenger, M.C.G.; Schindler, A.K. Modeling Hydration of Cementitious Systems. *ACI Mater. J.* **2012**, *109*, 225–234. [\[CrossRef\]](#)
54. Meinhard, K.; Lackner, R. Multi-Phase Hydration Model for Prediction of Hydration-Heat Release of Blended Cements. *Cem. Concr. Res.* **2008**, *38*, 794–802. [\[CrossRef\]](#)
55. Kolani, B.; Buffo-Lacarrière, L.; Sellier, A.; Escadeillas, G.; Boutillon, L.; Linger, L. Hydration of Slag-Blended Cements. *Cem. Concr. Compos.* **2012**, *34*, 1009–1018. [\[CrossRef\]](#)
56. Wang, X.-Y. Analysis of Hydration Kinetics and Strength Progress in Cement–Slag Binary Composites. *J. Build. Eng.* **2021**, *35*, 101810. [\[CrossRef\]](#)

57. Zeybek, Ö.; Özkılıç, Y.O.; Karalar, M.; Çelik, A.İ.; Qaidi, S.; Ahmad, J.; Burduhos-Nergis, D.D.; Burduhos-Nergis, D.P. Influence of Replacing Cement with Waste Glass on Mechanical Properties of Concrete. *Materials* **2022**, *15*, 7513. [[CrossRef](#)] [[PubMed](#)]
58. Kalakada, Z.; Doh, J.H.; Zi, G. Utilisation of Coarse Glass Powder as Pozzolanic Cement—A Mix Design Investigation. *Constr. Build. Mater.* **2020**, *240*, 117916. [[CrossRef](#)]
59. EN 197-1; Ciment—Partie 1: Composition, Spécifications et Critères de Conformité Des Ciments Courants. European Standard: Pilsen, Czech Republic, 2012.
60. NF EN 933-1; Essais Pour Déterminer Les Caractéristiques Géométriques Des Granulats—Partie 1: Détermination de La Granularité—Analyse Granulométrique Par Tamisage. European Standard: Pilsen, Czech Republic, 2012.
61. Kheir, J.; Hilloulin, B.; Loukili, A.; De Belie, N. Chemical Shrinkage of Low Water to Cement (w/c) Ratio CEM I and CEM III Cement Pastes Incorporating Silica Fume and Filler. *Materials* **2021**, *14*, 1164. [[CrossRef](#)]
62. Idir, R.; Cyr, M.; Tagnit-Hamou, A. Use of Fine Glass as ASR Inhibitor in Glass Aggregate Mortars. *Constr. Build. Mater.* **2010**, *24*, 1309–1312. [[CrossRef](#)]
63. Idir, R.; Cyr, M.; Tagnit-Hamou, A. Pozzolanic Properties of Fine and Coarse Color-Mixed Glass Cullet. *Cem. Concr. Compos.* **2011**, *33*, 19–29. [[CrossRef](#)]
64. Bordy, A.; Younsi, A.; Aggoun, S.; Fiorio, B. Cement Substitution by a Recycled Cement Paste Fine: Role of the Residual Anhydrous Clinker. *Constr. Build. Mater.* **2017**, *132*, 1–8. [[CrossRef](#)]
65. Jensen, O.M. Thermodynamic Limitation of Self-Desiccation. *Cem. Concr. Res.* **1995**, *25*, 157–164. [[CrossRef](#)]
66. Persson, B. Self-Desiccation and Its Importance in Concrete Technology. *Mater. Struct.* **1997**, *30*, 293–305. [[CrossRef](#)]
67. ASTM C230/230M; Standard Specification for Flow Table for Use in Tests of Hydraulic Cement. ASTM: West Conshohocken, PA, USA, 2014.
68. NF EN196-1; Methods of Testing Cement—Part 1: Determination of Strength. European Standard: Pilsen, Czech Republic, 2006.
69. AFPC-AFREM. *Durabilité Des Bétons: Méthodes Recommandées Pour La Mesure Des Grandeurs Associées à La Durabilité*; Laboratoire matériaux et durabilité des constructions, Institut national des sciences Appliquées, Université Paul Sabatier: Toulouse, France, 2009.
70. Kalpokaitė-Dičkuvienė, R.; Pitak, I.; Baltušnikas, A.; Lukošiuūtė, S.I.; Denafas, G.; Čėsniėnė, J. Cement Substitution by Sludge-Biomass Gasification Residue: Synergy with Silica Fume. *Constr. Build. Mater.* **2022**, *326*, 126902. [[CrossRef](#)]
71. Shah, R.; Pandit, R.K.; Gaur, M.K. Thermal Comfort Analysis through Development of Artificial Neural Network Models: An Experimental Study in Cwa Climate. *Mater. Today Proc.* **2022**, *57*, 2018–2025. [[CrossRef](#)]
72. al-Swaidani, A.M.; Khwies, W.T.; Al-Bali, M.; Lala, T. Development of Multiple Linear Regression, Artificial Neural Networks and Fuzzy Logic Models to Predict the Efficiency Factor and Durability Indicator of Nano Natural Pozzolana as Cement Additive. *J. Build. Eng.* **2022**, *52*, 104475. [[CrossRef](#)]
73. Di Benedetto, R.M.; Botelho, E.C.; Janotti, A.; Ancelotti Junior, A.C.; Gomes, G.F. Development of an Artificial Neural Network for Predicting Energy Absorption Capability of Thermoplastic Commingled Composites. *Compos. Struct.* **2021**, *257*, 113131. [[CrossRef](#)]
74. Gupta, P.; Sinha, N.K. Neural Networks for Identification of Nonlinear Systems: An Overview. In *Soft Computing and Intelligent Systems*; Elsevier: Amsterdam, The Netherlands, 2000; pp. 337–356.
75. Abirami, S.; Chitra, P. Energy-Efficient Edge Based Real-Time Healthcare Support System. *Adv. Comput.* **2020**, *117*, 339–368.
76. Menzies, T.; Kocagüneli, E.; Minku, L.; Peters, F.; Turhan, B. Using Goals in Model-Based Reasoning. In *Sharing Data and Models in Software Engineering*; Elsevier: Amsterdam, The Netherlands, 2015; pp. 321–353.
77. Davies, E.R. Biologically Inspired Recognition Schemes. In *Machine Vision*; Elsevier: Amsterdam, The Netherlands, 2005; pp. 725–755.
78. Yang, Z.R.; Yang, Z. Artificial Neural Networks. In *Comprehensive Biomedical Physics*; Elsevier: Amsterdam, The Netherlands, 2014; pp. 1–17.
79. Hallinan, J.S. Computational Intelligence in the Design of Synthetic Microbial Genetic Systems. *Methods Microbiol.* **2013**, *40*, 1–37.
80. Rajaorisoa, L. Large-Scale Building Thermal Modeling Based on Artificial Neural Networks: Application to Smart Energy Management. In *Artificial Intelligence Techniques for a Scalable Energy Transition*; Springer International Publishing: Cham, Switzerland, 2020; pp. 15–44.
81. Erway, J.B.; Marcia, R.F. On Solving Large-Scale Limited-Memory Quasi-Newton Equations. *Linear Algebra Appl.* **2017**, *515*, 196–225. [[CrossRef](#)]
82. Borhani, M. Multi-Label Log-Loss Function Using L-BFGS for Document Categorization. *Eng. Appl. Artif. Intell.* **2020**, *91*, 103623. [[CrossRef](#)]
83. Ali, M.M.M. Modified Limited-Memory Broyden-Fletcher-Goldfarb-Shanno Algorithm for Unconstrained Optimization Problem. *Indones. J. Electr. Eng. Comput. Sci.* **2021**, *24*, 1027. [[CrossRef](#)]
84. Nguyen, K.T.; Nguyen, Q.D.; Le, T.A.; Shin, J.; Lee, K. Analyzing the Compressive Strength of Green Fly Ash Based Geopolymer Concrete Using Experiment and Machine Learning Approaches. *Constr. Build. Mater.* **2020**, *247*, 118581. [[CrossRef](#)]
85. Naser, M.Z.; Thai, S.; Thai, H.-T. Evaluating Structural Response of Concrete-Filled Steel Tubular Columns through Machine Learning. *J. Build. Eng.* **2021**, *34*, 101888. [[CrossRef](#)]
86. Dung, C.V.; Anh, L.D. Autonomous Concrete Crack Detection Using Deep Fully Convolutional Neural Network. *Autom. Constr.* **2019**, *99*, 52–58. [[CrossRef](#)]
87. Cherif, R.; Hamami, A.E.A.; Ait-Mokhtar, A. Global Quantitative Monitoring of the Ion Exchange Balance in a Chloride Migration Test on Cementitious Materials with Mineral Additions. *Cem. Concr. Res.* **2020**, *138*, 106240. [[CrossRef](#)]
88. Adesina, A.; Das, S. Influence of Glass Powder on the Durability Properties of Engineered Cementitious Composites. *Constr. Build. Mater.* **2020**, *242*, 118199. [[CrossRef](#)]

89. Vance, K.; Aguayo, M.; Oey, T.; Sant, G.; Neithalath, N. Hydration and Strength Development in Ternary Portland Cement Blends Containing Limestone and Fly Ash or Metakaolin. *Cem. Concr. Compos.* **2013**, *39*, 93–103. [[CrossRef](#)]
90. Stepkowska, E.T.; Blanes, J.M.; Franco, F.; Real, C.; Pérez-Rodríguez, J.L. Phase Transformation on Heating of an Aged Cement Paste. *Thermochim. Acta* **2004**, *420*, 79–87. [[CrossRef](#)]
91. Damidot, D.; Lothenbach, B.; Herfort, D.; Glasser, F.P. Thermodynamics and Cement Science. *Cem. Concr. Res.* **2011**, *41*, 679–695. [[CrossRef](#)]
92. Ni, C.; Wu, Q.; Yu, Z.; Shen, X. Hydration of Portland Cement Paste Mixed with Densified Silica Fume: From the Point of View of Fineness. *Constr. Build. Mater.* **2021**, *272*, 121906. [[CrossRef](#)]
93. Lavergne, F.; Ben Fraj, A.; Bayane, I.; Barthélémy, J.F. Estimating the Mechanical Properties of Hydrating Blended Cementitious Materials: An Investigation Based on Micromechanics. *Cem. Concr. Res.* **2018**, *104*, 37–60. [[CrossRef](#)]
94. Scrivener, K.L.; Juilland, P.; Monteiro, P.J.M. Advances in Understanding Hydration of Portland Cement. *Cem. Concr. Res.* **2015**, *78*, 38–56. [[CrossRef](#)]
95. Bentz, D.P. Three-Dimensional Computer Simulation of Portland Cement Hydration and Microstructure Development. *J. Am. Ceram. Soc.* **1997**, *80*, 3–21. [[CrossRef](#)]
96. Kishi, T.; Maekawa, K. Multi-Component Model for Hydration Heat of Portland Cement. *Doboku Gakkai Ronbunshu* **1995**, *1995*, 97–109. [[CrossRef](#)] [[PubMed](#)]
97. Bullard, J.W.; Jennings, H.M.; Livingston, R.A.; Nonat, A.; Scherer, G.W.; Schweitzer, J.S.; Scrivener, K.L.; Thomas, J.J. Mechanisms of Cement Hydration. *Cem. Concr. Res.* **2011**, *41*, 1208–1223. [[CrossRef](#)]

Disclaimer/Publisher’s Note: The statements, opinions and data contained in all publications are solely those of the individual author(s) and contributor(s) and not of MDPI and/or the editor(s). MDPI and/or the editor(s) disclaim responsibility for any injury to people or property resulting from any ideas, methods, instructions or products referred to in the content.